The Stability of UV-Defluorination-Driven Crosslinked Carbon Nanotubes: A Raman Study

Yunxiang Gao *, Mohammad Tarequl Islam, Promise Uzoamaka Otuokere, Merlyn Pulikkathara, Yuemin Liu

Posted Date: 6 August 2024

doi: 10.20944/preprints202408.0406.v1

Keywords: fluorinated carbon nanotubes; defluorination; crosslinking; stability; Raman spectroscopy

Article

The Stability of UV-Defluorination-Driven Crosslinked Carbon Nanotubes: A Raman Study

Yunxiang Gao *, Mohammad Tarequl Islam, Promise Uzoamaka Otuokere, Merlyn Pulikkathara and Yuemin Liu

Department of Chemistry and Physics, Prairie View A&M University, Prairie View, TX 77446, USA
* Correspondence: yugao@pvamu.edu

Abstract: Carbon nanotubes (CNTs) can be considered as semi-rigid all-carbon polymers. However, unlike conventional polymers that can form 3D networks such as hydrogels or elastomers through crosslinking with each other in solution, the cylindrical carbon lattice of CNTs was not believed to be directly crosslinkable in solution until our recent discovery of UV-defluorination driven direct CNT crosslinking. In this study, we further reveal that the UV-defluorination-driven crosslinked CNTs are metastable and can decompose more readily than fluorinated or pristine CNTs upon exposure to Raman laser irradiation. Specifically, we investigate the stability of UV-defluorinated single-walled and multi-walled fluoro-nanotubes using Raman spectroscopy under controlled varying laser power. The results indicate that both the defluorinated single-walled and multi-walled CNTs are thermally less stable than pristine CNTs or untreated fluorinated CNTs, which can be attributed to the strains on the crosslinking bonds created from the curved carbon lattice of linked CNTs. This instability, particularly evident under high-power laser irradiation, leads to combustion processes ignited at relatively lower temperatures that cause an extended burned area centered on the laser spot, offering potential future applications as mechanically robust, lightweight materials with feasible post-use degradation options.

Keywords: fluorinated carbon nanotubes; defluorination; crosslinking; stability; Raman spectroscopy

1. Introduction

Carbon allotropes are conventionally classified into four categories based on the type of carbon lattice hybridization, including sp^3-hybridized diamond, sp^2-hybridized graphitic sheets (such as carbon nanotubes and graphene), fullerenes, and amorphous carbon [1]. The past decades have witnessed significant development in each type of carbon allotropes and their applications [2–4]. Some initial efforts have also been made to design hybrid carbon allotropes by merging existing ones, either through theoretical simulations [5–7] or experimental synthesis under extreme conditions [8,9]. For instance, carbon nanotubes (CNTs) have been crosslinked via their carbon lattice under extremely harsh conditions, including high temperatures (~2000 K), high pressures (tens of GPa), or high-energy beam bombardment [10–14] to form 3D sp^3-sp^2 hybrid carbon nano-allotropes.

In contrast to the harsh conditions needed for intertube crosslinking of CNTs, 0D fullerenes (represented by C_{60}) with higher lattice curvature can be effectively polymerized in solution under mild conditions with UV irradiation [15]. This distinct difference in the energy needed for self-polymerization is not only attributed to the lattice curvature strain [16] but also the fact that pristine CNTs are efficient free radical scavengers due to their large delocalized π-electron conjugation systems [17]. However, despite the "electron sea" on CNTs, single-walled carbon nanotubes (SWNTs) can be regarded as 1D polymers or 'the ultimate polymers' due to their structural definitions [18], physical behaviors in solution [19,20], and rheological properties [21,22]. These similarities to conventional polymers in physical properties, along with evidence of C_{60} photo-polymerization [15], led us to believe that disrupting the delocalized π-electron conjugation systems of CNTs might allow for polymerizing CNTs under relatively mild conditions. This hypothesis resulted in our recent success in crosslinking fully fluorinated single-walled carbon nanotubes (FSWNTs) directly via their

 doi:10.20944/preprints202408.0406.v1

carbon lattice at room temperature in solution [23]. This significant chemical property change is attributed to the full fluorination (or per-fluorination) of SWNTs, which completely disrupts the delocalized π-electron conjugation systems of the pristine SWNTs with a C/F ratio close to 2:1, or the simplest formula of C_2F [24]. The disruption turns conductive nanotubes into insulators, making them behave more like conventional polymers and allowing for the generation of localized reactive free radicals on the 'polymer chains' (here, the sidewall of carbon nanotubes) for crosslinking with each other [23]. As depicted in Figure 1A, reactive free radicals are generated and localized on the insulating sidewalls of FSWNTs via UV-defluorination at 254 nm, leading to direct intertube radical crosslinking of the defluorinated FSWNTs in solution or bundles.

The UV-crosslinked SWNTs may show unusual thermal stability due to their curved carbon lattice. A similar effect has been reported for the C_{60} dimer, C_{120}, which is much less stable and begins to decompose at only 150 °C due to the high curvature strain of the spherical C_{60} [25]. In moving from fullerenes to carbon nanotubes, the relatively reduced carbon lattice curvature may result in improved thermal stability compared to polymerized fullerenes, but they should be still metastable compared to individual CNTs without strained crosslinking sites. This assumption is set to be investigated in this study using Raman spectroscopy.

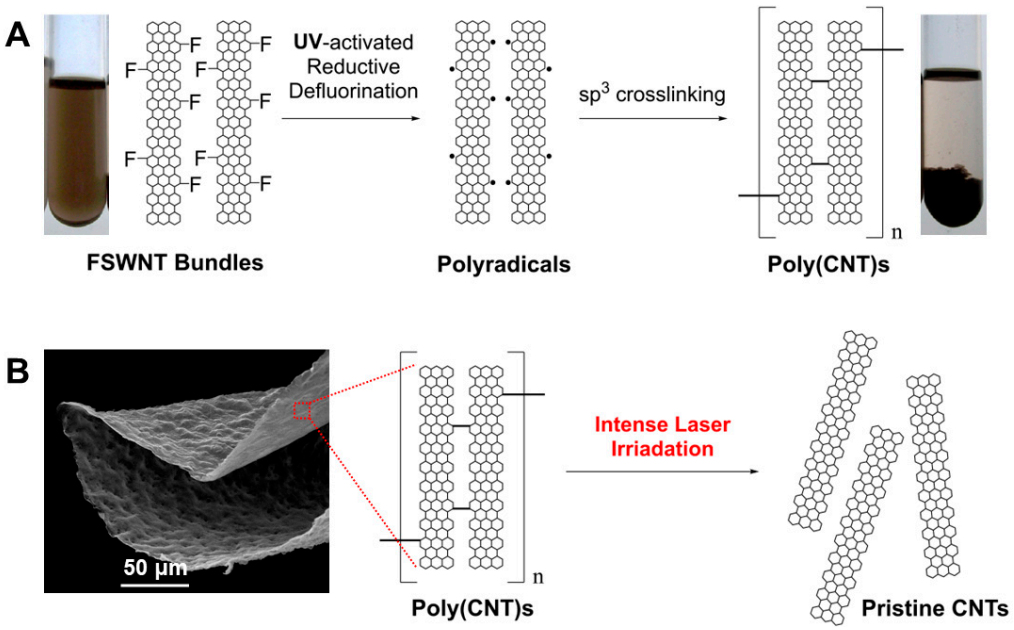

Figure 1. (A) Generation and recombination of free radicals in FSWNT bundles to form poly(CNTs), as described in our previous work [23]; (B) Thermal stability of crosslinked CNTs, the primary focus of the current study.

Raman spectroscopy is a leading tool for characterizing various carbon allotropes through the rotational and vibrational spectral signatures of carbon atoms in their lattice [26]. It is also widely used to assess the thermal stability and degradation of various materials due to its controllable laser power. Examples include Raman laser irradiation studies of red lead [27], synthetic magnetic nanoparticles [28], C_{60} nanowhiskers [29], perovskite nanocrystals [30], and pristine carbon nanotubes [31]. Here, we investigate the stability of UV-defluorination-driven crosslinked single-walled carbon nanotubes (**UV-DeF-SWNTs**) as well as multi-walled carbon nanotubes (**UV-DeF-MWNTs**) using Raman spectroscopy under controlled laser power. Our findings show that under gradually increased laser power, these UV-defluorinated CNTs undergo significant decomposition, with the crosslinked CNT structure reverting towards pristine CNTs (Figure 1B). More interestingly, at increased laser power, a combustion process of both UV-DeF-SWNTs and UV-DeF-MWNTs can be ignited at a lower energy than that required to ignite fluorinated CNTs and pristine CNTs, allowing their potential applications as mechanically robust, lightweight materials with feasible post-use removal options via burning off.

 doi:10.20944/preprints202408.0406.v1

2. Materials and Methods

2.1 Chemicals and Materials

Fluorinated single-walled carbon nanotubes (FSWNTs) with an approximate stoichiometry of C_2F_1 were purchased from Carbon Nanotechnologies, Inc. Fluorinated multi-walled carbon nanotubes (FMWNTs) were obtained from XFNano, Inc. Organic solvents, including 99.8% anhydrous *N, N*-Dimethylformamide (DMF) and 99.8% benzyl alcohol, were purchased from Fisher Scientific. All reagents were used as received.

2.2 Defluorination of Fluorinated Carbon Nanotubes

In a typical experiment, FSWNTs were defluorinated by exposing a DMF solution of FSWNTs (1 mg/mL) to 254 nm UV irradiation using a 5W Pen-Ray UV lamp in a photochemical micro-reactor (ACE Glasses) under Argon gas purging. After 2 hours of irradiation, the product precipitated out of the solution. This precipitate was collected by filtering the solution through a 0.22 μm pore size hydrophilic PVDF membrane filter to form a thin film, which was then rinsed with ethanol and acetone, and dried in a vacuum oven for subsequent analysis. Characterization techniques included transmission electron microscopy (TEM), energy dispersive X-ray analysis (EDX), Raman spectroscopy, and thermogravimetric analysis (TGA). The UV irradiation of FMWNTs was conducted under similar conditions, except using benzyl alcohol as the solvent and extending the UV irradiation time to 16 hours.

2.3 Characterization

TEM images were obtained using a Tecnai G2 F20 S-TWIN microscope operating at 200 kV. EDX analyses were conducted with a JEOL JSM-6010LA at 7 kV utilizing InTouchScope software. Raman spectra at 512 nm were recorded with a Thermo Fisher Scientific DXR Raman microscope over a range of 100–2000 cm^{-1}, with an adjustable power density of up to 2.9 kW/mm^2 and a 10X objective lens. Additionally, 633 nm Raman spectra were collected using a Jobin-Yvon LabRam HR 800 confocal micro-Raman system, with an adjustable power density of up to 4.2 kW/mm^2. For both wavelengths, spectra were typically acquired with a 10-second exposure time and 10 accumulations. TGA was performed in the air over a temperature range of 30–800 °C at a scanning rate of 10 °C/min using a TA Instruments TGA 2050 system. Approximately 6 mg of each sample was used, with platinum sample pans utilized for all experiments.

3. Results

Fluorinated carbon nanotubes dissolve in polar organic solvents due to their dipole interactions [32]. First, directly crosslinked SWNTs were prepared using UV irradiation at 254 nm in DMF solvent with inert Argon gas purging, as described in our previous work [23]. This photochemical treatment led to the precipitation of black floccule (Figure 1A), which could not be redispersed in any solvents, even with the assistance of surfactants, due to defluorination-induced intertube crosslinking. EDX analysis showed a significant decrease in fluorine content in UV-DeF-SWNTs, from 27.27% before to 2.23% after defluorination (Table 1). In contrast, the untreated FSWNT control sample, which underwent the same solution processing (dissolving, filtrating, drying) without UV irradiation, retained a higher fluorine content. TEM imaging further illustrates these changes, with the untreated FSWNT bundles exhibiting a cloudy appearance due to high fluorine surface functionalization (Figure 2A), whereas UV-DeF-SWNTs show clearer tubular structures due to the fluorine removal (Figure 2B).

 doi:10.20944/preprints202408.0406.v1

Table 1. EDX composition of FSWNT samples treated under various conditions.

Samples	Conditions	Composition (atom%)			
		C	O	F	N
FSWNTs	Untreated	68.23	3.98	27.79	0.00
UV-DeF-SWNTs	UV, 2 hrs.	92.66	5.11	2.23	0.00
HDZ-DeF-SWNTs	Hydrazine, 2 hr.	85.37	4.43	5.71	4.50

In general, Raman spectra of SWNTs feature three key bands: the Radial Breathing Mode (RBM), D-band, and G-band. The RBM band, observed in the low-frequency region (100-300 cm^{-1}), correlates with the nanotubes' diameter, offering insights into their size and chirality. The D-band, around 1350 cm^{-1}, signals defects and disorder within the carbon lattice, with a higher intensity indicating more diamond-like sp^3 hybridized carbon atoms or structural imperfections. The G-band, near 1580 cm^{-1}, corresponds to the tangential stretching mode of the carbon-carbon bonds in the sp^2 graphene-like carbon lattice of CNTs.

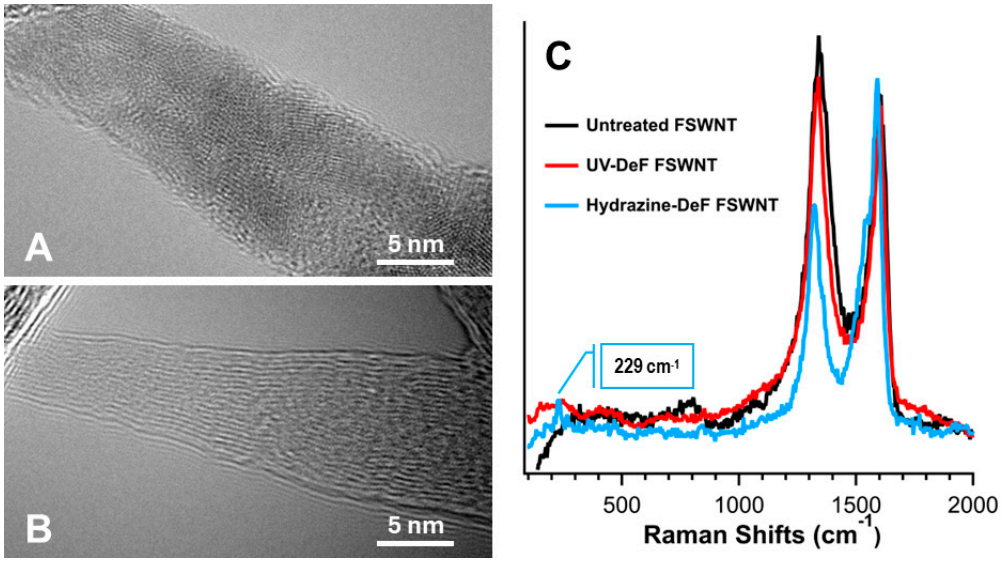

Figure 2. (A) TEM images of untreated fluorinated single-walled carbon nanotubes (FSWNTs) and (B) UV-crosslinked FSWNTs. (C) Raman spectra of untreated, UV-defluorinated, and hydrazine-defluorinated FSWNTs, recorded using a 532 nm laser wavelength with a power density of 2.9 kW/mm^2.

We performed Raman spectroscopy studies using a 532 nm laser at reduced power density (290 W/mm^2) for UV-DeF-SWNTs and untreated FSWNTs. For comparison, we also defluorinated FSWNTs using a different method reported by Mickelson *et al.*, which did not crosslink FSWNTs but instead recovered them towards individual pristine SWNTs [33]. Because this method involved using anhydrous hydrazine for FSWNT defluorination, we refer to the resulting product as "HDZ-DeF-SWNTs". Our Raman results showed that the HDZ-DeF-SWNTs exhibited spectral features of partially recovered individual SWNTs with a notable decrease in the D-band intensity at 1323 cm^{-1} and the reappearance of the RBM at 229 cm^{-1}, which is associated with the effective hydrazine-assisted defluorination (5.11% remaining fluorine by atom count, Table 1). In contrast, the UV-DeF-SWNTs yielded a Raman spectrum similar to that of the untreated FSWNTs, with neither significant D-band decrease at 1332 cm^{-1} nor the reappearance of the RBM, despite having even lower fluorine contents (2.23% by atom counts, Table 1) after the UV-Defluorination. This result aligns with the observation that UV-defluorination resulted in intertube crosslinking of neighboring SWNTs in their bundles after fluorine removal [23], which maintains the lattice disorder level and the D-band intensity.

 doi:10.20944/preprints202408.0406.v1

Carbon nanotubes are known for their exceptional thermal stability due to the strong sp^2 hybridization of carbon atoms in the carbon lattice, which provides high thermal conductivity and resistance to thermal degradation [34]. However, once polymerized, the formation of sp^3-sp^3 intertube carbon bonds between neighboring tubes introduces significant curvature strain, leading to potentially decreased thermal stability. To investigate this, we characterized UV-DeF-SWNTs using Raman spectroscopy under varying laser power, with untreated FSWNTs before UV irradiation as a control. Figure 3 shows their Raman spectra normalized at the G-band peak around 1599 cm^{-1}. The untreated FSWNTs showed no significant responses to the increased laser power from 1/10 to full (Figure 3A). In contrast, the crosslinked UV-DeF-SWNTs displayed a significant decrease in both the D-band intensity around 1340 cm^{-1} (Figure 3B) and the intensity ratio of the D-band to the G-band, I_D/I_G, with increased laser power (Figure 3C), indicating the thermal decomposition of the crosslinked SWNTs, reverting towards individual pristine tubes. This behavior is similar to the decomposition of strained crosslinking bonds observed in polymerized C_{60} under intense Raman laser irradiation [35].

Another significant difference was observed in the RBM band region (200-300 cm^{-1}), characteristic of the radial vibration of the carbon atoms in a perfectly cylindrical nanotube. Fluorination introduces sp^3 hybridization, distorting the cylindrical structure and making RBM bands absent in untreated FSWNTs (Figure 3A, 1/10 full power). These bands did not reappear in the control samples with increased laser power density (Figure 3A, inset). However, in the crosslinked UV-DeF-SWNTs, the RBM bands reappeared at higher laser power densities (Figure 3B, inset), consistent with the elimination of fluorine atoms and the decrease in the D-band, indicating a recovery towards pristine SWNTs.

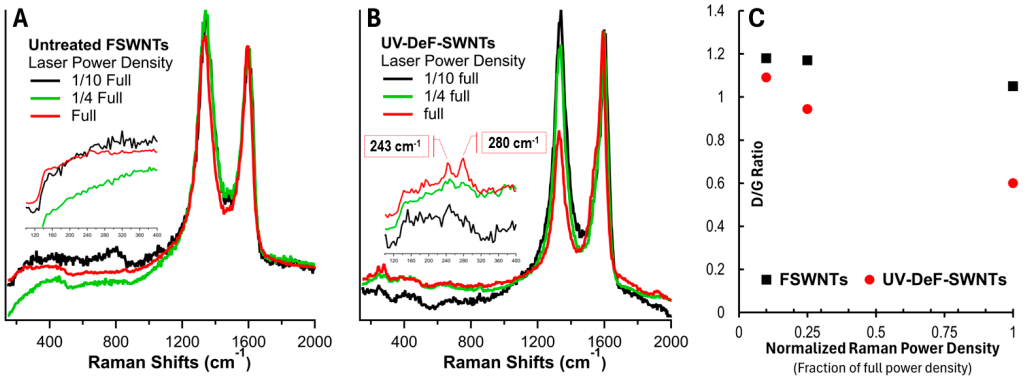

Figure 3. Raman spectra of (A) untreated FSWNTs and (B) UV-defluorinated crosslinked FSWNTs. (C) D/G ratio of untreated FSWNTs and UV-DeF-FSWNTs as a function of the fraction of full Raman laser power density. The Raman laser wavelength is 532 nm, with a full laser power density of 2.9 kW/mm^2. Insets in A and B show amplified RBM bands.

RBM bands also provide diameter information, as the RBM frequency (ω_{RBM}) is inversely proportional to the nanotube diameter (d_t), following the relation $\omega_{RBM} = 248/d_t$ [36]. The inset in Figure 3B shows that at full laser power, UV-DeF-SWNT samples exhibited distinct RBM peaks at 280 and 243 cm^{-1}, corresponding to diameters of 0.88 nm and 0.98 nm, respectively. The Kataura plot correlates SWNT diameters with their electronic properties and chiralities. Under 532 nm laser excitation (2.33 eV), peaks between 275 and 200 cm^{-1} (0.90 ~ 1.24 nm in diameter) are from metallic nanotubes, while those above 275 cm^{-1} (below 0.90 nm in diameter) are from semiconducting tubes [37]. Thus, the 243 cm^{-1} peak in Figure 3B indicates metallic tubes, and the 280 cm^{-1} peak represents semiconducting tubes. Interestingly, under 1/4 full laser power, the metallic RBM peak at 243 cm^{-1} was stronger than the semiconducting peak at 280 cm^{-1}, however, the semiconducting peak increased significantly at full power, suppressing the metallic peak. This suggests that metallic SWNTs decompose and recover more readily than semiconducting ones in the crosslinked SWNT bundles or networks, being consistent with observations in pristine SWNTs, where metallic tubes are more prone to Raman laser damage than semiconducting tubes [38]. This behavior is likely due to the

 doi:10.20944/preprints202408.0406.v1

higher density of free electrons in metallic SWNTs, which enhances electron-phonon coupling and photon energy absorption, leading to more localized heating and increased structural instability.

The RBM frequency of each individual SWNT is not directly altered by the laser excitation wavelength, but the excitation wavelength does determine which chiralities of SWNTs are activated, selectively enhancing certain RBM frequencies in the Raman spectrum. Thus, we further analyzed the UV-DeF-SWNT and untreated FSWNT samples using 633 nm laser excitation at varied laser power densities. Figure 4 shows that untreated FSWNTs exhibited no significant changes across different laser power densities (Figure 4A). In contrast, the crosslinked UV-DeF-SWNTs showed a significant decrease in D-band intensity (Figure 4B) and the I_D/I_G ratio (Figure 4C) with increasing laser power density, indicating the thermal decomposition of the crosslinked SWNTs and their recovery towards individual pristine tubes.

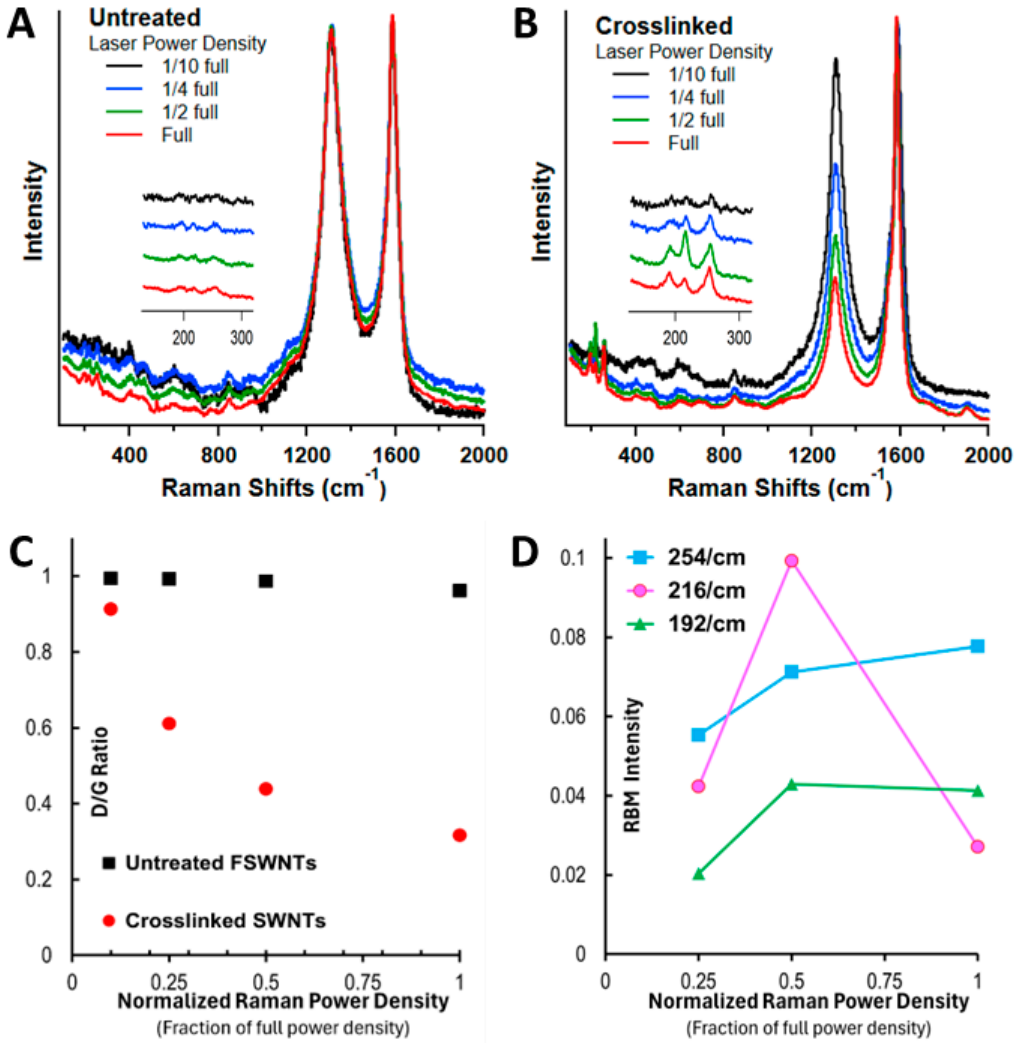

Figure 4. Raman spectra of (A) untreated FSWNTs and (B) crosslinked FSWNTs via defluorination, using a 633 nm laser at varying power densities. (C) D/G ratio of untreated and crosslinked FSWNTs as a function of the fraction of full laser power density. (D) Changes in RBM peak intensity in response to increasing laser power density. Full power density: 4.2 kW/mm².

RBM bands also did not reappear in untreated FSWNTs when using 633 nm laser excitation across all applied laser power densities (Figure 4A, inset). However, in UV-DeF-SWNTs, RBM bands emerged at 254, 216, and 192 cm^{-1} at increased power, corresponding to 0.98, 1.15, and 1.29 nm diameter tubes, respectively (Figure 4B, inset). According to the Kataura plot, at 633 nm excitation (1.96 eV), RBM bands below 225 cm^{-1} indicate metallic nanotubes, while those above 225 cm^{-1} are from semiconducting nanotubes [39]. Applying this to our 633 nm Raman results, the RBM peaks at

 doi:10.20944/preprints202408.0406.v1

216 and 192 cm^{-1} correspond to metallic SWNTs, and the peak at 254 cm^{-1} to semiconducting SWCNTs. The intensity of the semiconducting peak at 254 cm^{-1} continuously increased with rising laser power (Figure 4D), consistent with the behavior observed with a 532 nm laser, suggesting that the recovered semiconducting SWNTs from the laser thermal decomposition survived under increased laser power. In contrast, the RBM peak intensity of metallic SWNTs at 216 and 192 cm^{-1} initially increased with power density from 1/10 to 1/2 but started to decrease when the laser power further reached full. This indicates that metallic tubes are more easily decomposed from the crosslinked state, reverting to individual pristine SWNTs, and that they are more susceptible to damage from Raman laser irradiation than semiconducting tubes [38]. Notably, the peak intensity of the smaller diameter metallic tubes at 216 cm^{-1} decreased faster than that of the larger metallic tubes at 192 cm^{-1}, agreeing with previous findings that smaller diameter pristine metallic nanotubes are more prone to thermal degradation [40].

During the Raman spectroscopy characterization, we captured microscope images of the sample areas irradiated by the Raman laser. As shown in Figure 5, A1 and A2 are the images of pristine SWNTs irradiated with a 532 nm Raman laser at 1/10 of the full power and at full power, respectively. There was no visible damage to the pristine SWNTs, even at full laser power. In contrast, for untreated FSWNTs, no damage was observed at 1/10 laser power (Figure 5, B1); however, a hole was drilled at full power due to stronger thermal effects (Figure 5, B2). The size of the burned area was approximately 2 μm, nearly matching the laser spot size, indicating that pristine SWNTs have higher thermal stability than fluorinated ones. Interestingly, although the crosslinked UV-DeF-SWNTs also showed no burning spot at 1/10 power density (Figure 5, C1), the burned area was significantly larger than the laser spot size at full power density (Figure 5, C2). This suggests that the laser may have ignited the crosslinked SWNTs, causing the burned area to expand rapidly, which is likely due to the Raman characterization performed in the presence of air.

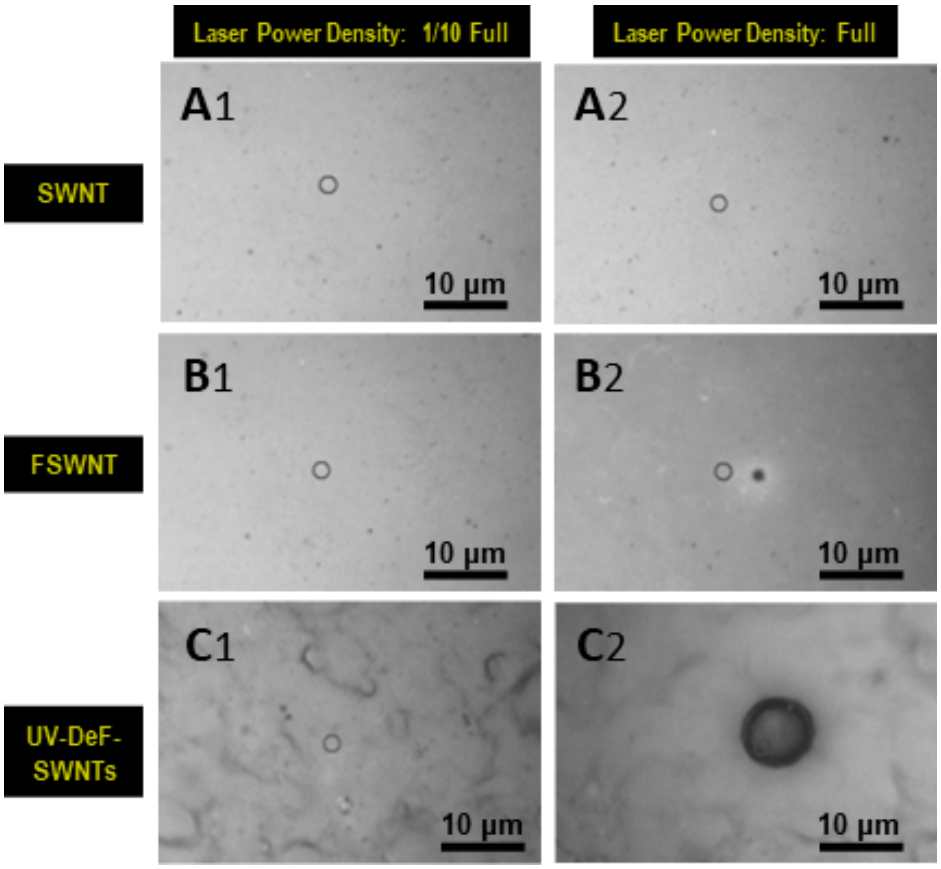

Figure 5. Microscope images of the Raman laser-irradiated sample areas: (A1, A2) pristine SWNTs, (B1, B2) untreated FSWNTs, and (C1, C2) crosslinked UV-DeF-SWNTs irradiated at 1/10 (Column 1) and full (Column 2) power density, respectively. Full power density: 2.9 kW/mm^2.

 doi:10.20944/preprints202408.0406.v1

Following the study on fluorinated single-walled carbon nanotubes, we extended the work to fluorinated multi-walled carbon nanotubes (FMWNTs) using the same UV irradiation method and Raman characterization techniques. We found that the UV irradiation of FMWNTs only resulted in partial defluorination. We note the product of these UV-defluorinated FMWNTs as UV-DeF-MWNTs. As shown in Table 2, the fluorine content decreased from 44.18% by atom counts in the untreated FMWNT samples to 28.42% in UV-DeF-MWNTs after 16 hours of UV exposure, representing a loss of approximately 48% of its original fluorine contents after calibrating the total atom number in UV-DeF-MWNTs by considering the loss of fluorine. This indicates that the FMWNT defluorination is significantly less efficient than the near-complete defluorination observed in FSWNTs, where fluorine content decreased to 2.23% within just 2 hours of UV irradiation. The lower and slower defluorination rate in FMWNTs is likely due to the less pronounced curvature of MWNTs' carbon lattice compared to the highly curved SWCNTs [41]. Additionally, similar to FSWNTs, FMWNTs showed a slight increase in oxygen content post-UV-irradiation, which could be attributed to the presence of O_2 contaminants in an imperfect solvation system [42] or trace amounts of water from polar organic solvents [43].

Table 2. SEM-EDX composition of FMWNT samples treated under various conditions.

Samples	Conditions	Composition (atom%)		
		C	O	F
FMWNTs	Untreated	54.15	1.67	44.18
UV-DeF-MWNTs	UV, 16 hrs.	66.59	4.99	28.42

We characterized the untreated FMWNTs and UV-DeF-MWNTs using 532 nm Raman spectroscopy. It's normal for MWNTs that the RBM bands are naturally absent because the motion of the outer tubes is highly constrained by the multilayer interactions with the inner graphitic layers. Therefore, we only used the intensity ratio of the D-band to the G-band, I_D/I_G, as a measure of the degree of defects in MWNT-related samples.

As shown in Figure 6A,B, with the G-band normalized to 1 and the laser power density reduced to 1/10 of full power to avoid thermal damage, both untreated and UV-fluorinated FMWNTs exhibited a similar I_D/I_G ratio of 1.4. For MWNTs, the I_D/I_G ratio typically increases after surface chemical functionalization and decreases when MWNTs recover towards their pristine state [44]. Thus, compared to the untreated FMWNTs, the unchanged I_D/I_G ratio of UV-Def-FWNTs after 48% fluorine elimination indicates that the defluorination process did not primarily restore sp^2 bonding within the carbon lattice but rather aligns with the formation of intertube crosslinked sp^3 carbon bonds.

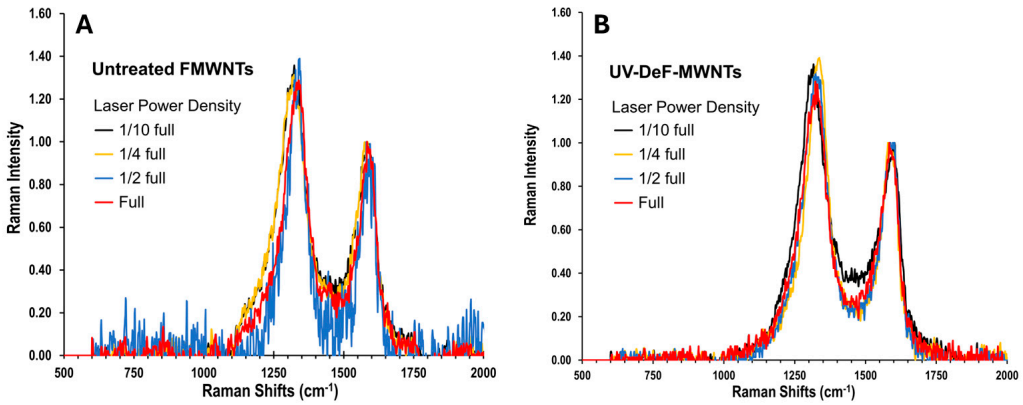

Figure 6. Raman spectra of (A) untreated FMWNTs and (B) UV-Defluorinated FMWNT (UV-DeF-MWNTs). Laser wavelength: 532 nm, with a full power density of 2.9kW/mm^2.

 doi:10.20944/preprints202408.0406.v1

When the Raman laser power was increased, untreated FMWNTs did not show a decrease in the D-band intensity across the laser power range from 1/10 full to full (Figure 6A), similar to the behavior observed in untreated FSWNTs (Figure 3A). Notably, UV-DeF-MWNTs also did not show a decrease in the D-band intensity within the same power density range (Figure 6B), which differs from the response seen in UV-DeF-SWNTs, indicating higher thermal stability of UV-DeF-MWNTs compared to that of UV-DeF-SWNTs due to the reduced curvature strain on MWNTs.

MWNTs, due to their multi-layer coherent structure, are more rigid than SWNTs. This rigidity causes MWNT films prepared by the filtration procedure to show less resistance to shrinkage during the solvent drying process, resulting in a more uneven film surface under a microscope. In Figure 7, A1 and A2 show the microscopic images of pristine MWNTs irradiated with a 532 nm Raman laser at 1/10 full power and full power, respectively. There was no visible damage to the pristine MWNTs, even at full laser power (Figure 7, A2). For untreated FMWNTs, both spots exposed to 1/10 power density (Figure 7, B1) and full power density (Figure 7, B2) exhibited small burning spots equivalent to the laser spot size, indicating that fluorinated MWNTs have less thermal stability than their pristine counterparts. Comparatively, FMWNTs showed a drilled hole under 1/10 of full power, whereas FSWNTs exhibited almost no damage under the same conditions, suggesting that the commercially available FMWNTs used in this study were slightly less thermally stable than FSWNTs. This is likely due to the higher fluorination level in the commercially available untreated FMWNTs (44.18% F) compared to that of FSWNTs (27.79% F), resulting in a higher defect level that reduces the thermal stability of carbon nanotubes more significantly.

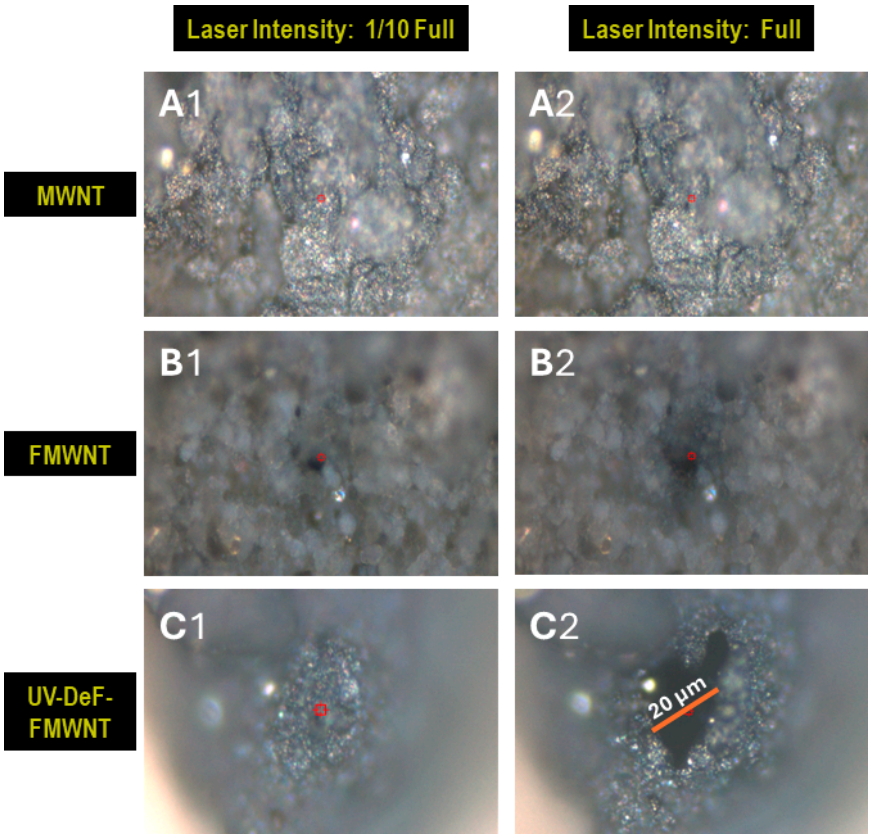

Figure 7. Microscope images of various MWNTs irradiated with a 532 nm Raman laser at 1/10 full power density (Left, Column 1) and full power density (Right, Column 2). (A) Pristine MWNTs, (B1) Untreated FMWNTs, and (C) UV-defluorinated MWNTs (UV-DeF-MWNTs).

On the other hand, for UV-DeF-MWNTs, although laser radiation at 1/10 power did not cause noticeable damage to the samples (Figure 7, C1), at full laser power, the laser-burned area was significantly larger than the laser spot size (Figure 7, C2), suggesting that the laser may have ignited combustion in the UV-DeF-MWNT sample, causing the burning area to expand rapidly. To confirm

 doi:10.20944/preprints202408.0406.v1

the occurrence of combustion, we performed TGA in air, anticipating that the TGA curve may show a sudden change when combustion is ignited. For example, a rapid rise in the sample temperature may potentially outpace the instrument's programmed heating rate, resulting in a temperature spike, and after the exothermic event (when the combustion process stops), the temperature returns to the temperature-increasing baseline set by the heating program.

As expected, small bumps were observed in the TGA curve of UV-DeF-MWNTs slightly above 500 °C, indicating rapid exothermic processes, while for untreated FSWNTs, such bumps were not observed until the temperature went beyond 600 °C (Figure 8). These TGA features align with the observation that full-power UV-irradiation of untreated FSWNTs did not result in a larger damaged area (Figure 7, B2), whereas the same irradiation on UV-DeF-MWNTs produced a significantly larger burnt area than the actual laser spot size (Figure 7, C2). Notably, these TGA bumps suggest exothermic processes causing a temperature spike without a corresponding sharp mass loss. This can be attributed to the solid packing of nanotubes during the filtration-based membrane sample preparation. Combustion on the film surface that was exposed to the air sufficiently raised the temperature of the sample to cause sharp temperature spikes in the TGA curve, but mass loss is a slower process due to the tight filtration-packing. After these exothermic events, the TGA curves returned to the programmed heating-rate-controlled temperature baseline, forming the bumps featured in the TGA curve (Figure 8B). Based on the first combustion-related TGA-bump, the UV-DeF-MWNTs can be ignited at significantly lower temperatures by about 100 °C, compared to untreated FSWNTs.

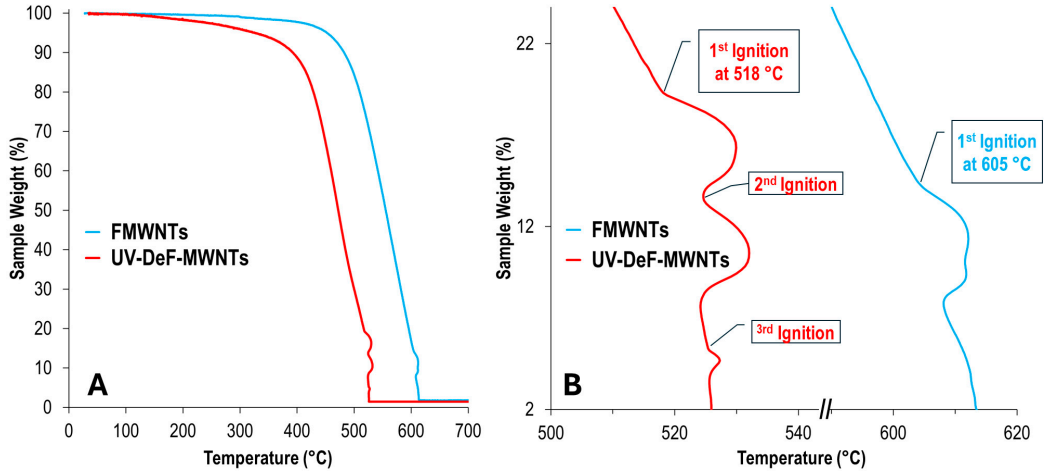

Figure 8. (A) TGA curves of FMWNTs and UV-DeF-MWNTs. (B) Enlarged view of the ignition and combustion region featured in (A).

4. Conclusions

In summary, this study has characterized the thermal stability of crosslinked carbon nanotubes prepared using a UV-defluorination method reported in our previous work. Both single-walled and multi-walled carbon nanotubes were examined. Raman spectroscopy revealed that UV irradiation of fluorinated single-walled carbon nanotubes effectively eliminated fluorine. The resulting UV-DeF-SWNT product exhibited features consistent with intertube crosslinking, rather than restoring back to pristine SWNTs, thus maintaining a higher degree of disorder feature in Raman spectra. However, the UV-defluorination process for fluorinated multi-walled carbon nanotubes was less efficient, achieving only partial defluorination. This reduced efficiency is due to the lower curvature of MWNTs' carbon lattice, which results in less strain and increased thermal stability of the C-F bonds.

Raman spectroscopy with controlled laser power density showed that both UV-DeF-SWNTs and UV-DeF-MWNTs were stable under reduced laser power but began to decompose with increased laser power. Notably, unlike pristine or untreated fluorinated carbon nanotubes, the UV-defluorinated nanotubes exhibited signs of combustion when exposed to full laser power, which was not observed in the other samples under the same conditions. Thermogravimetric analysis of UV-

 doi:10.20944/preprints202408.0406.v1

DeF-MWNTs showed small combustion bumps at temperatures above 518 °C, almost 100 °C lower than that of untreated FMWNTs, indicating a reduced energy for post-use materials removal due to the easier decomposition of the metastable crosslinked sites, which aligns well with the larger burn areas observed under full power Raman laser irradiation compared to pristine CNTs or untreated fluorinated CNTs. Overall, these findings suggest that UV-defluorinated carbon nanotubes are metastable compared to pristine or fluorinated carbon nanotubes, whether single-walled or multi-walled.

This work redefines the role of carbon nanotubes from being just 'polymer-like' in terms of their physical properties to being chemically crosslinkable and degradable 'real polymers'. The ability to directly crosslink CNTs under ambient conditions in solution and subsequently degrade them under specific conditions, such as intense laser irradiation, enables their potential applications as macroscopic carbon allotropes for light yet robust mechanical reinforcement, with lower energy-cost removal as a post-use option.

Author Contributions: Conceptualization, Y.G.; methodology, Y.G.; synthesis, Y.G., M.T.I., and P.U.O.; Characterization and data analysis, Y.G., M.P., M.T.I. and Y.L.; writing and draft preparation, Y.G.; supervision, Y.G.; project administration, Y.G.; funding acquisition, Y.G.

Funding: This research was funded by the USDA-NIFA 1890 Land Grant Institution Capacity Building Grants (CBG) Program, grant number 1028570. Any opinions, findings, conclusions, or recommendations expressed in this material are those of the authors and do not necessarily reflect the views of the USDA-NIFA.

Data Availability Statement: We encourage all authors of articles published in MDPI journals to share their research data. In this section, please provide details regarding where data supporting reported results can be found, including links to publicly archived datasets analyzed or generated during the study. Where no new data was created, or where data is unavailable due to privacy or ethical restrictions, a statement is still required. Suggested Data Availability Statements are available in section "MDPI Research Data Policies" at https://www.mdpi.com/ethics.

Conflicts of Interest: The authors declare no conflicts of interest. The funders had no role in the design of the study; in the collection, analyses, or interpretation of data; in the writing of the manuscript; or in the decision to publish the results.

References

1. Tiwari, S.K.; Kumar, V.; Huczko, A.; Oraon, R.; Adhikari, A.D.; Nayak, G.C. Magical Allotropes of Carbon: Prospects and Applications. *Crit Rev Solid State Mater Sci* **2016**, *41*, 257-317, doi:10.1080/10408436.2015.1127206.
2. De Volder, M.F.L.; Tawfick, S.H.; Baughman, R.H.; Hart, A.J. Carbon Nanotubes: Present and Future Commercial Applications. *Science* **2013**, *339*, 535-539, doi:10.1126/science.1222453.
3. Geim, A.K.; Novoselov, K.S. The rise of graphene. *Nat Mater* **2007**, *6*, 183-191, doi:10.1038/Nmat1849.
4. Gao, Y.; Zhang, L.; Xia, Z.; Li, C.M.; Dai, L. Hole-punching for enhancing electrocatalytic activities of 2D graphene electrodes: Less is more. *J Chem Phys* **2020**, *153*, doi:10.1063/5.0012709.
5. Ovid'ko, I.A. Review on Grain Boundaries in Graphene. Curved Poly- and Nanocrystalline Graphene Structures as New Carbon Allotropes. *Rev Adv Mater Sci* **2012**, *30*, 201-224.
6. Zhang, S.H.; Zhou, J.; Wang, Q.; Chen, X.S.; Kawazoe, Y.; Jena, P. Penta-graphene: A new carbon allotrope. *PNAS* **2015**, *112*, 2372-2377, doi:10.1073/pnas.1416591112.
7. Wang, Z.H.; Zhou, X.F.; Zhang, X.M.; Zhu, Q.; Dong, H.F.; Zhao, M.W.; Oganov, A.R. Phagraphene: A Low-Energy Graphene Allotrope Composed of 5-6-7 Carbon Rings with Distorted Dirac Cones. *Nano Lett* **2015**, *15*, 6182-6186, doi:10.1021/acs.nanolett.5b02512.
8. Chalifoux, W.A.; Tykwinski, R.R. Synthesis of polyynes to model the sp-carbon allotrope carbyne. *Nat Chem* **2010**, *2*, 967-971, doi:10.1038/Nchem.828.
9. Lin, Y.; Zhang, L.; Mao, H.K.; Chow, P.; Xiao, Y.M.; Baldini, M.; Shu, J.F.; Mao, W.L. Amorphous Diamond: A High-Pressure Superhard Carbon Allotrope. *Phys Rev Lett* **2011**, *107*, doi:10.1103/Physrevlett.107.175504.
10. Khabashesku, V.N.; Gu, Z.N.; Brinson, B.; Zimmerman, J.L.; Margrave, J.L.; Davydov, V.A.; Kashevarova, L.S.; Rakhmanina, A.V. Polymerization of single-wall carbon nanotubes under high pressures and high temperatures. *J Phy Chem B* **2002**, *106*, 11155-11162, doi: 10.1021/JP025983W
11. Terrones, M.; Terrones, H.; Banhart, F.; Charlier, J.C.; Ajayan, P.M. Coalescence of single-walled carbon nanotubes. *Science* **2000**, *288*, 1226-1229, doi: 10.1126/SCIENCE.288.5469.1226

12. Kis, A.; Csanyi, G.; Salvetat, J.P.; Lee, T.N.; Couteau, E.; Kulik, A.J.; Benoit, W.; Brugger, J.; Forro, L. Reinforcement of single-walled carbon nanotube bundles by intertube bridging. *Nat Mater* **2004**, *3*, 153-157, doi:10.1038/nmat1076
13. Jaroenapibal, P.; Luzzi, D.E.; Evoy, S. Tuning the resonant frequency of single-walled carbon nanotube bundle oscillators through electron-beam-induced cross-link formations. *Appl Phys Lett* **2007**, *90*, 081912, doi:10.1063/1.2472535
14. Peng, B.; Locascio, M.; Zapol, P.; Li, S.Y.; Mielke, S.L.; Schatz, G.C.; Espinosa, H.D. Measurements of near-ultimate strength for multiwalled carbon nanotubes and irradiation-induced crosslinking improvements. *Nat Nanotechnol* **2008**, *3*, 626-631, doi: 10.1038/nnano.2008.211
15. Sun, Y.P.; Ma, B.; Bunker, C.E.; Liu, B. All-carbon polymers (polyfullerenes) from photochemical reactions of fullerene clusters in room-temperature solvent mixtures. *J Am Chem Soc* **1995**, *117*, 12705-12711, doi:10.1021/Ja00156a007.
16. Lin, T.; Zhang, W.-D.; Huang, J.; He, C. A DFT Study of the Amination of Fullerenes and Carbon Nanotubes: Reactivity and Curvature. *J Phys Chem B* **2005**, *109*, 13755-13760, doi:10.1021/jp051022g.
17. Galano, A. Carbon nanotubes: promising agents against free radicals. *Nanoscale* **2010**, *2*, 373-380, doi:10.1039/b9nr00364a.
18. Green, M.J.; Behabtu, N.; Pasquali, M.; Adams, W.W. Nanotubes as polymers. *Polymer* **2009**, *50*, 4979-4997, doi:10.1016/j.polymer.2009.07.044.
19. Yao, Y.B.; Luo, S.D.; Liu, T. Determination of the Length, Diameter, Molecular Mass, Density and Surfactant Adsorption of SWCNTs in Dilute Dispersion by Intrinsic Viscosity, Sedimentation, and Diffusion Measurements. *Macromolecules* **2014**, *47*, 3093-3100, doi:10.1021/ma5003497.
20. Parra-Vasquez, A.N.G.; Duque, J.G.; Green, M.J.; Pasquali, M. Assessment of length and bundle distribution of dilute single-walled carbon nanotubes by viscosity measurements. *AIChE J* **2014**, *60*, 1499-1508, doi:10.1002/aic.14325.
21. Tsentalovich, D.E.; Ma, A.W.K.; Lee, J.A.; Behabtu, N.; Bengio, E.A.; Choi, A.; Hao, J.; Luo, Y.M.; Headrick, R.J.; Green, M.J.; et al. Relationship of Extensional Viscosity and Liquid Crystalline Transition to Length Distribution in Carbon Nanotube Solutions. *Macromolecules* **2016**, *49*, 681-689, doi:10.1021/acs.macromol.5b02054.
22. Shen, Z.; Roding, M.; Kroger, M.; Li, Y. Carbon Nanotube Length Governs the Viscoelasticity and Permeability of Buckypaper. *Polymers* **2017**, *9*, doi:10.3390/Polym9040115.
23. Gao, Y.X.; Chen, H.W.; Ge, J.; Zhao, J.N.; Li, Q.W.; Tang, J.X.; Cui, Y.; Chen, L.W. Direct Intertube Cross-Linking of Carbon Nanotubes at Room Temperature. *Nano Lett* **2016**, *16*, 6541-6547, doi:10.1021/acs.nanolett.6b03184.
24. Bettinger, H.F. Experimental and Computational Investigations of the Properties of Fluorinated Single-Walled Carbon Nanotubes. *ChemPhysChem* **2003**, *4*, 1283-1289, doi:10.1002/cphc.200300854.
25. Zhang, J.Y.; Porfyrakis, K.; Sambrook, M.R.; Ardavan, A.; Briggs, G.A.D. Determination of the thermal stability of the fullerene dimers C_{120}, $C_{120}O$, and $C_{120}O_2$. *J Phys Chem B* **2006**, *110*, 16979-16981, doi:10.1021/jp062506v.
26. Thapliyal, V.; Alabdulkarim, M.E.; Whelan, D.R.; Mainali, B.; Maxwell, J.L. A concise review of the Raman spectra of carbon allotropes. *Diam Relat Mater* **2022**, *127*, 109180, doi:10.1016/j.diamond.2022.109180.
27. Li, Y.; Ma, J.; He, K.; Wang, F. Raman Study of 532-Nanometer Laser-Induced Degradation of Red Lead. *Materials* **2024**, *17*, 770, doi: 10.3390/ma17040770
28. Restelli, S.; Albini, B.; Bonomi, S.; Bini, M.; Mozzati, M.C.; Galinetto, P. Raman study of the laser-induced decomposition of ZnFe2O4 nanoparticles. *Mater Today Commun* **2023**, *35*, doi:10.1016/J.Mtcomm.2023.106405.
29. Kato, R.; Miyazawa, K.i. Raman Laser Polymerization of C_{60} Nanowhiskers. *J Nanotechnol* **2012**, *2012*, 101243, doi:10.1155/2012/101243.
30. Liao, M.; Shan, B.; Li, M. In Situ Raman Spectroscopic Studies of Thermal Stability of All-Inorganic Cesium Lead Halide ($CsPbX_3$, X = Cl, Br, I) Perovskite Nanocrystals. *J. Phys. Chem. Lett.* **2019**, *10*, 1217–1225. doi: 10.1021/acs.jpclett.9b00344
31. Mases, M.; Noel,M.; Dossot, M.; McRae, E.; Soldatov, A. V. Laser-induced damage and destruction of HiPCO nanotubes in different gas environments. *Phys. Status Solidi B* **2011**, *248*, 2540 —2543, doi: 10.1002/pssb.201100136
32. Liu, Y.; Zhang, Y.C.; Wang, Z.M.; Lai, W.C.; Zhang, X.J.; Wang, X.; Liu, X.Y. Investigation of the dispersion behavior of fluorinated MWCNTs in various solvents. *Phys Chem Chem Phys* **2017**, *19*, 21565-21574, doi:10.1039/c7cp04536k.
33. Mickelson, E.T.; Huffman, C.B.; Rinzler, A.G.; Smalley, R.E.; Hauge, R.H.; Margrave, J.L. Fluorination of single-wall carbon nanotubes. *Chem Phys Lett* **1998**, *296*, 188-194, doi: 10.1016/s0009-2614(98)01026-4
34. Gupta, N.; Gupta, S.M.; Sharma, S.K. Carbon nanotubes: synthesis, properties and engineering applications. *Carbon Lett* **2019**, *29*, 419-447, doi:10.1007/s42823-019-00068-2.

35. Sakai, M.; Ichida, M.; Nakamura, A. Photopolymerization and thermal decomposition of polymerized phase in C_{60} crystals under strong laser illumination. *Fullerene Sci Techn* **2001**, *9*, 351-361, doi: 10.1081/fst-100104499
36. Kneipp, K.; Perelman, L.T.; Kneipp, H.; Backman, V.; Jorio, A.; Dresselhaus, G.; Dresselhaus, M.S. Coupling and scattering power exchange between phonon modes observed in surface-enhanced Raman spectra of single-wall carbon nanotubes on silver colloidal clusters. *Phys Rev B* **2001**, *63*, 193411, doi:10.1103/PhysRevB.63.193411.
37. Kataura, H.; Kumazawa, Y.; Maniwa, Y.; Umezu, I.; Suzuki, S.; Ohtsuka, Y.; Achiba, Y. Optical properties of single-wall carbon nanotubes. *Synth Met* **1999**, *103*, 2555-2558, doi:10.1016/S0379-6779(98)00278-1.
38. Huang, H.J.; Maruyama, R.; Noda, K.; Kajiura, H.; Kadono, K. Preferential destruction of metallic single-walled carbon nanotubes by laser irradiation. *J Phys Chem B* **2006**, *110*, 7316-7320, doi:10.1021/jp056684k.
39. Maultzsch, J.; Telg, H.; Reich, S.; Thomsen, C. Radial breathing mode of single-walled carbon nanotubes: Optical transition energies and chiral-index assignment. *Phys Rev B* **2005**, *72*, 205438, doi:10.1103/PhysRevB.72.205438.
40. Corio, P.; Santos, P.S.; Pimenta, M.A.; Dresselhaus, M.S. Evolution of the molecular structure of metallic and semiconducting carbon nanotubes under laser irradiation. *Chem Phys Lett* **2002**, *360*, 557-564, doi:10.1016/S0009-2614(02)00866-7.
41. Zhang, W.; Dubois, M.; Guerin, K.; Bonnet, P.; Kharbache, H.; Masin, F.; Kharitonov, A.P.; Hamwi, A. Effect of curvature on C-F bonding in fluorinated carbons: from fullerene and derivatives to graphite. *Phys Chem Chem Phys* **2010**, *12*, 1388-1398, doi:10.1039/b914853a.
42. Bettinger, H.F.; Peng, H. Thermolysis of Fluorinated Single-Walled Carbon Nanotubes: Identification of Gaseous Decomposition Products by Matrix Isolation Infrared Spectroscopy. *J Phys Chem B* **2005**, *109*, 23218-23224, doi:10.1021/jp054370r.
43. Bulusheva, L.G.; Fedoseeva, Y.V.; Okotrub, A.V.; Flahaut, E.; Asanov, I.P.; Koroteev, V.O.; Yaya, A.; Ewels, C.P.; Chuvilin, A.L.; Felten, A.; et al. Stability of Fluorinated Double-Walled Carbon Nanotubes Produced by Different Fluorination Techniques. *Chem Mater* **2010**, *22*, 4197-4203, doi:10.1021/cm100677c.
44. Judek, J.; Jastrzebski, C.; Malolepszy, A.; Mazurkiewicz, M.; Stobinski, L.; Zdrojek, M. Laser induced temperature effects in multi-walled carbon nanotubes probed by Raman spectroscopy. *Phys Status Solidi A* **2012**, *209*, 313-316, doi:10.1002/pssa.201127586.